Available online at www.sciencedirect.com
SCIENCE DIRECT®
Acta Materialia xxx (2004) xxx–xxx
Acta MATERIALIA
www.actamat-journals.com

Compression behavior of porous NiTi shape memory alloy

Ying Zhao [a,*], Minoru Taya [a], Yansheng Kang [b], Akira Kawasaki [b]

[a] Department of Mechanical Engineering, Center for Intelligent Materials and Systems, University of Washington, P.O. Box 352600, Seattle, WA 981952600, USA
[b] Department of Materials Processing, Faculty of Engineering, Tohoku University, Sendai 980-8790, Japan

Received 2 March 2004; received in revised form 30 July 2004; accepted 17 September 2004

Abstract

Porous NiTi alloy with several different porosities was processed by spark plasma sintering. The compression behavior of the porous NiTi was examined with the aim of using it possibly as a high energy absorbing material. A model for the macroscopic compression behavior of porous shape memory alloy (SMA) is presented in this work, where Eshelby's inhomogeneous inclusion method is used to predict the effective elastic and superelastic behavior of a porous SMA based on the assumption of stress–strain curve. The analytical results are compared with experimental data for porous NiTi with 13% porosity, resulting in a reasonably good agreement.

Keywords: Porous NiTi; Eshelby's method; Compression behavior; Spark plasma sintering

1. Introduction

Over the last two decades shape memory alloys (SMA) have attracted great interest in various applications ranging from aerospace [1] and naval [2] to surgical instruments, medical implants and fixtures [3,4]. The use of SMAs has promoted extensive research on developing SMA constitutive models.

Among SMAs, NiTi alloy has been used most extensively due to its large flow stress and shape memory effect (SME) strain. Most recently, porous NiTi have attracted increasing attention for possible application in medical implant devices and as high energy absorption structural material. The progress in manufacturing and characterization of the porous NiTi SMA has been reported by a number of researchers [5–9]. Li et al. [5,6] fabricated porous NiTi SMA by combustion synthesis method, the stress–strain curves in their work show that the porous NiTi synthesized by this method is brittle. Li et al. [7] also fabricated the porous NiTi from powder sintering; they show that there is no stress plateau in the stress–strain curve and the material is still brittle. Kim et al. [8] produced porous NiTi by self-propagating high temperature synthesis (SHS), and again the porous NiTi fabricated by this method is brittle. Lagoudas et al. [9] used the hot isostatic press (HIP) method. The stress–strain curve in their work exhibits brittle behavior. Since these previous studies on porous NiTi exhibited poor ductility, it is necessary for us to develop a better processing method which provides porous NiTi with higher ductility. Therefore, the spark plasma sintering (SPS) method [10] is introduced in this work. The pre-alloy NiTi raw powders of superelastic grade (Ni 50.9 at.%–Ti 49.1 at.%) are loaded into a graphite die and pressed to the desired pressure and then a huge on-off pulsed current is induced through the die and stacked powder particles. Under the condition of pulsed current heating, powder particles are activated to a high energy

* Corresponding author. Tel.: +1 206 616 2163; fax: +1 206 616 4088.
E-mail address: yzhao@u.washington.edu (Y. Zhao).

1359-6454/$30.00 © 2004 Published by Elsevier Ltd on behalf of Acta Materialia Inc.
doi:10.1016/j.actamat.2004.09.029

state and neck formation easily occurs at low temperature in very short time compared with ordinary sintering processes like hot press (HP), HIP or SHS. Moreover, the effect of spark discharge purifies the surface of powder particles, which guarantees neck formation and high quality of sintered materials. The above features of SPS meet our demand for preparing porous NiTi using NiTi alloy powders.

In order to optimally design the microstructure and properties of the porous SMAs, it is important to build a simple, yet accurate model to describe its microstructure–mechanical behavior relation. If a porous NiTi is treated as a special case of a particle-reinforced composite, one can apply a micromechanical model based on Eshelby's method with Mori–Tanaka mean-field (MT) theory [11–17] and self-consistent method [18,19]. Both methods have been used to model macroscopic behavior of composites with SMA fibers [20,21]. Young's modulus of a porous material was modeled by using the Eshelby's method with MT theory [22].

In this paper, Eshelby's equivalent inclusion method with Mori–Tanaka mean-field theory is used to predict the stress–strain (SS) curve of a porous NiTi under compression where the superelastic deformation corresponding to the second stage of the SS curve is accounted for. Then the predicted SS curve is compared with the experimental data of the porous NiTi specimen processed by SPS.

2. Experimental results of NiTi specimens processed by SPS

We have processed three different types of specimens by spark plasma sintering (Dr. Sinter SPS-515S, Sumitomo Coal Mining Co., Japan). Fig. 1 is a schematic drawing of the SPS device. An ingot of NiTi alloy (Ni 50.9 at.% and Ti 49.1 at.%) was made by Sumitomo Metals, Osaka, Japan, which was then shipped to Fukuda Metals, Kyoto, Japan, where the plasma rotating electrode process (PREP) was used to process NiTi powders. The average diameter of the NiTi powders processed by PREP is 150 μm. The advantage of SPS is to provide strong bonding among superelastic grade NiTi powders while the relatively low sintering temperature is maintained for only 5 min, thus avoiding any undesired reaction products that would be produced by a conventional sintering method. A summary of three types of specimens is given in Table 1. All these specimens were subjected to the same heat treatment (320 °C, 30 min, water quench) to convert them to superelastic grade. Their transformation temperatures were measured from differential scanning calorimeter chart (Perkin–Elmer, DSC6 model): A_s (austenite start), A_f (austenite finish), M_s (martensite start) and M_f (martensite finish).

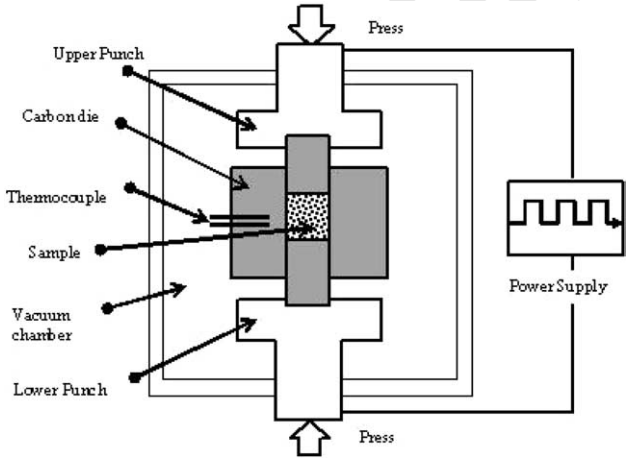

Fig. 1. A schematic drawing of SPS device.

The porosity of the specimens was measured by the formula, $f_p = 1 - m/(\rho V)$, where V and m is the volume and mass of the porous specimen, respectively. The density ρ in this work is the density of NiTi, i.e. 6.4 g/cm^3 as measured by the mass–density relation, i.e. $\rho = m_D/V_D$, the unit of ρ is g/cm^3, where V_D and m_D is the volume and mass of the dense NiTi specimen, respectively. The porous specimens had a functionally graded microstructure (FGM), i.e. NiTi powders of smaller size are purposely distributed near the top and bottom surfaces while the larger sized NiTi powders are located in mid-thickness region, Fig. 2. The 13% porosity NiTi specimen exhibited continuous NiTi phase throughout the thickness directions with porosity centered at mid-plane (Fig. 2(b)) while in the 25% porosity specimen porosity is distributed through the thickness, with less towards the top and bottom surfaces (Fig. 2(a)).

Two kinds of compressive tests were conducted by using Instron tensile frame (8521 model System) to obtain the stress–strain curves of both dense and porous NiTi. Two different testing temperatures were used: room temperature (22 °C) and a temperature 15–25 °C higher than the austenite finish temperature (A_f). The porous specimens with porosity of 13% and 25% as well as the dense specimen were all tested under static compressive load (loading rate 10^{-5} s^{-1}).

2.1. Compressive curves of NiTi SMA at room temperature (22 °C)

Specimens were cut by electrical discharge machining (EDM) from the as-SPS processed disks. As-EDM cut specimens were all subjected to the same heat treatment (320 °C, for 30 min, water quenched) to convert them to superelastic grade. Fig. 3 shows the compressive stress–strain curves of 13%, 25% porosity and dense (no porosity) specimens. Among those curves, the 25% porosity exhibits lowest flow

Table 1
NiTi specimens processed by spark plasma sintering

Name of sample	Porosity by volume percentage	Spark plasma processing conditions	Transformation temperatures (°C)
Dense NiTi	0	850 °C under 50 MPa, 5 min	$A_s = 23.88$, $A_f = 43.12$ $M_s = 36.05$, $M_f = 23.09$
13% porous NiTi	13%	800 °C under 25 MPa, 5 min	$A_s = 19.3$, $A_f = 38.82$ $M_s = 20.65$, $M_f = 5.39$
25% porous NiTi	25%	750 °C under 5 MPa, 5 min	$A_s = 14.59$, $A_f = 33.29$ $M_s = 23.24$, $M_f = 2.55$

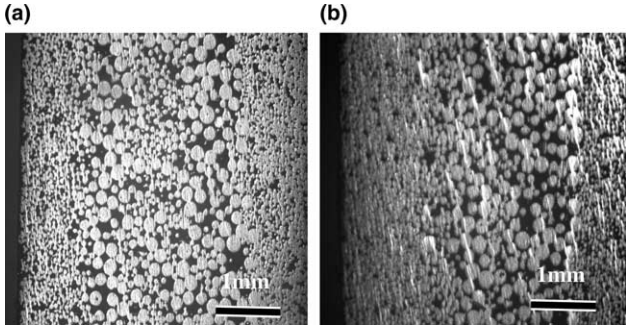

Fig. 2. Microstructure of porous NiTi specimens: (a) 25% porosity; (b) 13% porosity.

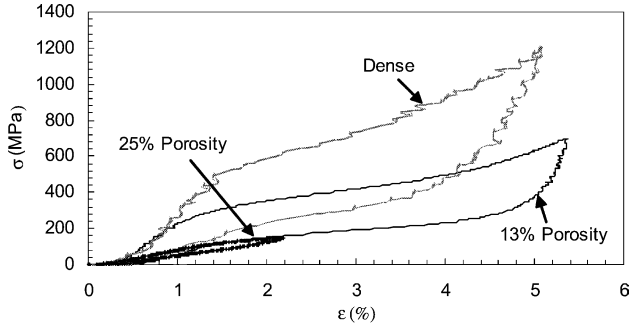

Fig. 3. Compressive stress–strain curve of specimens tested at room temperature.

stress level and less superelastic loop behavior, while both the 13% porosity and dense specimens clearly exhibit large superelastic loops and also high ductility. The main reason for good superelastic behavior of the 13% porosity NiTi specimen processed by SPS is the rather continuous connectivity between adjacent NiTi powders of SE grade in the high porosity region (mid-section). In the case of the 25% porosity NiTi specimen, such connectivity is not established in the mid-section, i.e. there is non-uniform connectivity. In addition, presumably some large NiTi powder particles are clustered, some of which may have converted to unwanted brittle intermetallics; this would have been caused by excess local high temperature during the SPS process. When stress is large enough, collapse of imperfect necking structure among large NiTi particles of 25% porosity exhibits low strength rather than superelastic property. From the results of the compression testing, we selected the 13% porosity specimen as a representative porous NiTi while the dense specimen is used as a reference NiTi processed by the same SPS.

Fig. 4(a)–(c) are the optical micrographs of the side section view of 13% porosity specimen before compression test, and those tested up to 5% compressive strain and unloaded, and 7% compressive strain and unloaded. If these micrographs are referred to the compressive stress–strain curves of Fig. 3, Fig. 4(a) and (b) correspond to the compressive strains of 0% and 5%, respectively, and the superelastic strain of up to 5% was actually realized as shown by Fig. 4(b). Fig. 4(c) demonstrates the plastic deformation of particles in the 13% porosity specimen that was loaded up to 7% and then unloaded. This is due to the martensitic phase. The results of Fig. 4 support the assumption that superelastic NiTi powder in the SPS-processed and heat treated condition deforms superelastically, contributing to the high

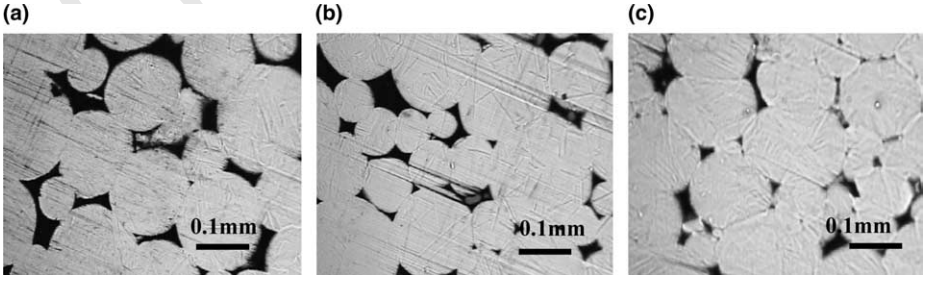

Fig. 4. Side view of 13% porosity: (a) before compression; (b) compressed up to 5% and unloaded; (c) compressed up to 7% and unloaded.

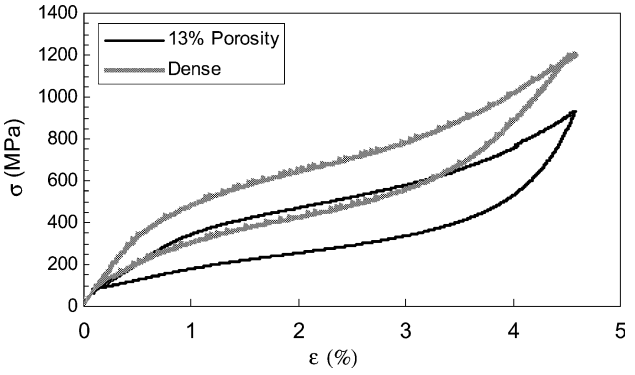

Fig. 5. Compressive stress–strain curves of 13% porosity and dense samples tested at 58 °C.

ductility of the porous NiTi. On the other hand, the microstructure of the 25% porosity samples is not as sound as that of the 13% porosity ones; the compressive stress–strain curve of the 25% porosity NiTi exhibits much lower flow stress.

2.2. Compressive stress–strain curves of dense and 13% porosity specimens tested at temperature higher than A_f

Both 13% porosity and dense specimens are tested under compression at testing temperature higher than their austenite finish temperatures. The compressive stress–strain curves of the 13% porosity and dense NiTi specimens are given in Fig. 5. The compressive stress–strain curves tested at $T > A_f$ (Fig. 5) more clearly exhibit a superelastic loop at higher flow stress level than that for those tested at room temperature (Fig. 3). This is due to the fact that NiTi exhibits superelastic behavior at higher flow stress level more obviously at a higher testing temperature.

3. Modeling of the compressive stress–strain curves of porous NiTi

This model assumes piecewise linear SS curve of superelastic NiTi. This idealized SS curve is illustrated in Fig. 7, where the first linear part A_iB_i corresponds to the elastic loading of 100% austenite phase, the second linear part B_iD_i is the stress-induced martensite transformation plateau, D_id_i is unloading of 100% martensite phase, d_ib_i is the reverse transformation lower plateau, final linear part is b_iA_i, elastic unloading of 100% austenite phase. The subscript 'i' in Fig. 7 denotes dense (i = D) or porous NiTi (i = P). The stress–strain curve consists of two portions; one is the loading curve, and the other is the unloading curve. First we will model the loading curve, and then the unloading curve is simulated in the same manner as the loading curve.

3.1. Loading curve

The compressive stress–strain curve of 13% porosity specimen of Fig. 5 exhibits three stages: first stage A_iB_i (100% austenite phase); second stage upper plateau B_iD_i (stress-induced martensite phase); and third stage D_id_i (100% martensite phase). Although the compressive stress–strain curves for these three stages are not piecewise linear, we assume in the second model that in each stage it is linear. Then we attempt to simulate three piecewise linear portions by a simple model based on Eshelby's effective medium model with Mori–Tanaka mean-field theory. Let us denote the slopes of the linearized first, second and third stages of porous NiTi are E_{M_s}, E_T and E_{M_f}, respectively, where the subscripts M_s, T and M_f, respectively, denote the first stage with martensite start (equivalently 100% austenite phase), the second linearized slopes with tangent modulus and the third stage with martensite finish, i.e. 100% martensite phase. The stresses at the transition between the first and second stages and between the second and third stages are denoted by $\sigma^P_{M_s}$ and $\sigma^P_{M_f}$, respectively, where the superscript 'P' denotes the porous NiTi. Therefore, the calculation of the moduli E_{M_s}, E_T and E_{M_f} as well as the martensitic transformation start stress $\sigma^P_{M_s}$ and martensitic transformation finish stress $\sigma^P_{M_f}$ is the key in this modeling work. It is noted in the second model that no uniform strain and stress in the matrix NiTi is assumed.

3.1.1. Critical stresses

The start and finish martensitic transformation stresses $\sigma^P_{M_s}$, $\sigma^P_{M_f}$ can be obtained by the relation in Eq. (1) as

$$\sigma^P_{M_s} = (1 - f_p)\sigma^D_{M_s}, \tag{1a}$$

$$\sigma^P_{M_f} = (1 - f_p)\sigma^D_{M_f}, \tag{1b}$$

where $\sigma^D_{M_s}$ and $\sigma^D_{M_f}$ are, respectively, the start and finish martensitic transformation stress that are averaged in the matrix domain.

3.1.2. Stiffness of the first and third stages

Mochida et al. [22] obtained the formula based on Eshelby's model with Mori–Tanaka mean-field theory to calculate the Young's modulus of a porous material is given by

$$\frac{E^P}{E^D} = \frac{1}{1 + \eta f_p}, \tag{2}$$

where for spherical pores, η is given by

$$\eta = \frac{15}{7(1 - f_p)}. \tag{3}$$

Brief derivation of Eqs. (2) and (3) is given in Appendix A.

3.1.3. Stiffness of the second stage

The Young's modulus (E) of a NiTi with transformation ε_T is estimated by

$$E(\varepsilon_T) = E_A + \frac{\varepsilon_T}{\bar{\varepsilon}}(E_M - E_A), \tag{4}$$

where E_A, E_M are the Young's modulus of 100% austenite and 100% martensite phase, respectively, Fig. 6, and $\bar{\varepsilon}$ is the maximum transformation strain, and it is given by

$$\bar{\varepsilon} = \varepsilon_{M_f} - \frac{\sigma_{M_f}}{E_M}. \tag{5}$$

Eq. (4) is valid for both dense and porous NiTi, thus we can rewrite Eq. (4) using Eq. (5) as

$$E^i = E^i_A - \frac{E^i_A - E^i_M}{\varepsilon^i_{M_f} - \sigma^i_{M_f}/E^i_M}\varepsilon_T, \tag{6}$$

where the superscript 'i' denotes i = D (dense) or P (porous). In order to obtain the slope of the linearized second stage of compressive stress–strain curve of a porous NiTi, we consider the equivalency of strain energy density. However, in the case of the second stage, the macroscopic strain energy density of a porous NiTi should be evaluated from the trapezoidal area of Fig. 7, i.e. $B_iC_iF_iH_i$, where i = P for an arbitrary transformation strain ε^P_T. Therefore, the macroscopic strain energy density of porous NiTi with ε^P_T calculated graphically from Fig. 8 is given by

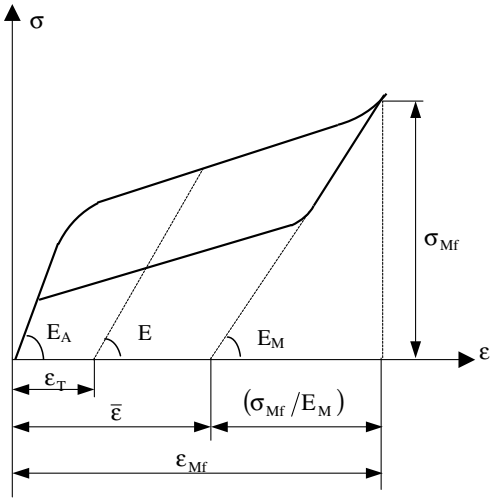

Fig. 6. Stress–strain curve of porous or dense sample.

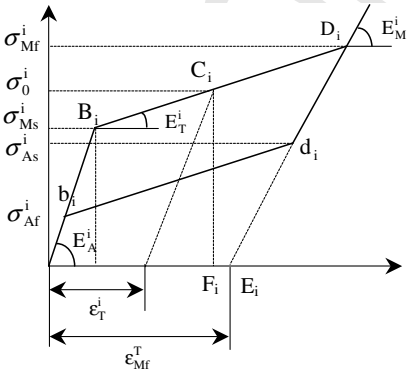

Fig. 7. Idealized stress–strain curve with three stages (subscript or superscript 'i' denotes either porous or dense NiTi).

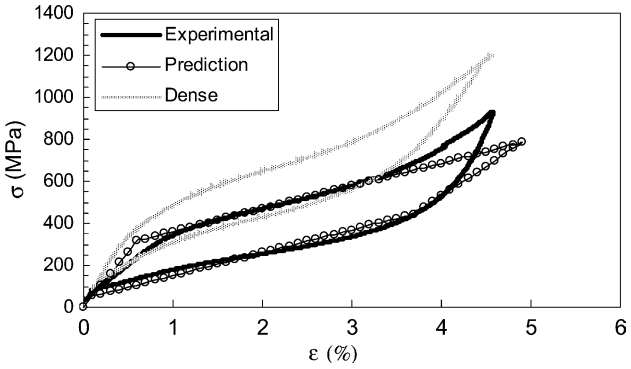

Fig. 8. Comparison of model and experimental stress–strain curves.

$$W = \frac{1}{2}\left(\sigma^P_{M_s} + \sigma^P_0\right)\left(\varepsilon^P_T + \frac{\sigma^P_0}{E_{AM}} - \frac{\sigma^P_{M_s}}{E_{M_s}}\right), \tag{7}$$

where $\sigma^P_{M_s}$ is the start martensitic transformation stress of porous NiTi composite, σ^P_0 is an applied stress, ε^P_T is the strain corresponding to σ^P_0, Fig. 7. Since there is no transformation strain in pores, the transformation strain for porous NiTi ε^P_T is the uniform transformation strain in the matrix i.e. dense NiTi, ε^D_T,

$$\varepsilon^P_T = \varepsilon^D_T \equiv \varepsilon_T. \tag{8}$$

The above macroscopic strain energy density is set equal to the microscopic strain energy density that is calculated from the Eshelby's inhomogeneous inclusion method [11,12]

$$W = \frac{1}{2}\mathbf{C}^{m-1}_{ijkl}\sigma^0_{ij}\sigma^0_{kl} + \frac{1}{2}f_p\sigma^0_{ij}\varepsilon^*_{kl}, \tag{9}$$

where the corresponding Eshelby's problem provides the solution for ε^*_{ij} as

$$\varepsilon^*_{kl} = \varepsilon^T_{kl} - \frac{1}{1-f_p}(\mathbf{S}_{klmn} - \mathbf{I})^{-1}C^{m-1}_{ijkl}\sigma^0_{ij}. \tag{10}$$

Substituting Eq. (10) into Eq. (9), the microscopic strain energy density, W is given by

$$W = \frac{1}{2}\sigma^0_{ij}\varepsilon^0_{ij} + \frac{1}{2}f_p\sigma^0_{ij}\left[2\varepsilon^T_{ij} - \frac{1}{1-f_p}(\mathbf{S}_{ijkl} - \mathbf{I})^{-1}\varepsilon^0_{kl}\right]. \tag{11}$$

Since the porous NiTi is subjected to uniaxial load, i.e. $\sigma^0_{ij} = \{0\ 0\ \sigma^P_0\ 0\ 0\ 0\}^T$, and $\varepsilon^T_{ij} = \{v\varepsilon_T\ v\varepsilon_T\ -\varepsilon_T\ 0\ 0\ 0\}^T$ and the pores are assumed to be spherical, thus Eq. (11) can be reduced to

$$W = \frac{1}{2}\sigma^P_0\varepsilon_0 + \frac{1}{2}f_p\sigma^P_0\left[2\varepsilon_T + \frac{15}{7(1-f_p)}\varepsilon_0\right], \tag{12}$$

where ε_0 is the macroscopic strain of the porous NiTi, and it is related to applied stress σ_0^{P} as

$$\varepsilon_0 = \frac{\sigma_0^{\mathrm{P}}}{E_{\mathrm{AM}}}. \tag{13}$$

Substituting Eq. (13) into Eq. (12), the microscopic strain energy density W of porous NiTi is finally reduced to

$$W = \frac{1}{2}\frac{\left(\sigma_0^{\mathrm{P}}\right)^2}{E_{\mathrm{AM}}} + \frac{1}{2}f_{\mathrm{p}}\sigma_0^{\mathrm{P}}\left[2\varepsilon_{\mathrm{T}}^{\mathrm{P}} - \frac{15}{7(1-f_{\mathrm{p}})}\frac{\sigma_0^{\mathrm{P}}}{E_{\mathrm{AM}}}\right], \tag{14}$$

where E_{AM} is the Young's modulus of dense (matrix) NiTi with ε_{T}.

By equating the macroscopic strain energy density Eq. (7) to the microscopic strain energy density Eq. (14), and using Eq. (6) with i = P, we obtained an algebraic equation of second-order in terms of ε_{T} as

$$A(\varepsilon_{\mathrm{T}})^2 + B\varepsilon_{\mathrm{T}} + C = 0, \tag{15}$$

where

$$A = \frac{(\gamma\sigma_0^{\mathrm{P}} + \sigma_{M_{\mathrm{s}}}^{\mathrm{P}})(1-\beta)}{\varepsilon_{M_{\mathrm{s}}}},$$

$$B = \gamma\sigma_0^{\mathrm{P}} + \sigma_{M_{\mathrm{s}}}^{\mathrm{P}} + \frac{\sigma_{M_{\mathrm{s}}}^{\mathrm{P}}(1-\beta)(\sigma_{M_{\mathrm{s}}}^{\mathrm{P}} + \sigma_0^{\mathrm{P}})}{E_{M_{\mathrm{s}}}\varepsilon_{M_{\mathrm{f}}}},$$

$$C = \frac{(1-\alpha)(\sigma_0^{\mathrm{P}})^2 - (\sigma_{M_{\mathrm{s}}}^{\mathrm{P}})^2}{E_{M_{\mathrm{s}}}}$$

and

$$\alpha = 1 - \frac{f_{\mathrm{p}}}{1-f_{\mathrm{p}}}(\mathbf{S}_{3333} - 1)^{-1}, \quad \beta = \frac{E_{M_{\mathrm{f}}}}{E_{M_{\mathrm{s}}}}, \quad \gamma = 1 - 2f_{\mathrm{p}}.$$

Solve for $\varepsilon_{\mathrm{T}}^{\mathrm{P}}$ that corresponds to the second kink point, D_{P}, in Fig. 7

$$\varepsilon_{\mathrm{T}} = \frac{-B + \sqrt{B^2 - 4AC}}{2A}. \tag{16}$$

The tangent modulus of the porous NiTi is the slope of the second portion of the stress–strain curve shown in Fig. 7, thus, E_{T} can be expressed in terms of transformation strain and the stresses

$$E_{\mathrm{T}} = \frac{\sigma_0^{\mathrm{P}} - \sigma_{M_{\mathrm{s}}}^{\mathrm{P}}}{\varepsilon_{\mathrm{T}}}. \tag{17}$$

3.2. Unloading curve

During unloading, the porous NiTi material undergoes transformation (martensite phase to austenite phase). Before the applied stress reaches the critical value $\sigma_{A_{\mathrm{s}}}^{\mathrm{P}}$, the matrix NiTi remains 100% martensite phase (first stage of the unloading SS curve in the modeling curve). When the applied stress is decreased to $\sigma_{A_{\mathrm{s}}}^{\mathrm{P}}$, reverse transformation starts. The reverse transformation finishes when the stress reaches another critical value $\sigma_{A_{\mathrm{f}}}^{\mathrm{P}}$, thereafter the porous NiTi material remains 100% austenite. Therefore, the slopes of the first and third stages of the unloading curve are the Young's modulus of the 100% martensite and 100% austenite phase, respectively. The slope of the second stage is the same as that of the loading curve. Therefore, the Young's moduli of the unloading curve are related to those of the loading curve as

$$E_{A_{\mathrm{s}}} = E_{M_{\mathrm{f}}}, \tag{18a}$$

$$E_{\mathrm{T}}^{\mathrm{u}} = E_{\mathrm{T}}, \tag{18b}$$

$$E_{A_{\mathrm{f}}} = E_{M_{\mathrm{s}}}, \tag{18c}$$

where $E_{\mathrm{T}}^{\mathrm{u}}$ is the slope of the second stage of the unloading curve. The superscript 'u' denotes unloading where those without superscript are the slopes of loading curve.

The start and finish austenite transformation stresses of porous NiTi $\sigma_{A_{\mathrm{s}}}^{\mathrm{P}}$ and $\sigma_{A_{\mathrm{f}}}^{\mathrm{P}}$ are related to the corresponding stresses of the dense NiTi and

$$\sigma_{A_{\mathrm{s}}}^{\mathrm{P}} = (1-f_{\mathrm{p}})\sigma_{A_{\mathrm{s}}}^{\mathrm{D}}, \tag{19a}$$

$$\sigma_{A_{\mathrm{f}}}^{\mathrm{P}} = (1-f_{\mathrm{p}})\sigma_{A_{\mathrm{f}}}^{\mathrm{D}}, \tag{19b}$$

where $\sigma_{A_{\mathrm{s}}}^{\mathrm{D}}$ and $\sigma_{A_{\mathrm{f}}}^{\mathrm{D}}$ are start and finish austenite transformation stresses of the dense NiTi, respectively. First we assume that the dense NiTi matrix is isotropic with Poisson's ratio $\nu^{\mathrm{A}} = \nu^{\mathrm{M}} = 0.33$. The input data which are measured from the idealized compressive stress–strain curve of Fig. 5 are shown in Table 2.

Table 2
Input data

$\sigma_{M_{\mathrm{s}}}^{\mathrm{D}}$ (MPa)	$\sigma_{M_{\mathrm{f}}}^{\mathrm{D}}$ (MPa)	$\sigma_{A_{\mathrm{f}}}^{\mathrm{D}}$ (MPa)	E_{A} (GPa)	E_{M}	$\varepsilon_{M_{\mathrm{s}}}$	$\varepsilon_{M_{\mathrm{f}}}$
400	720	300	75	31	0.004	0.032

4. Conclusion

Porous and solid NiTi specimens are processed by spark plasma sintering where two different porosities are used, 13% and 25%. The 13% porosity NiTi appears to possess a sound microstructure with high ductility while the 25% porosity NiTi specimens exhibit much lower stress flow than that of the 13% porosity.

Then the compressive stress–strain curve of the 13% porosity NiTi is simulated by a model which is based on piecewise linear stress–strain curve. This model predicts the piecewise SS curve with the flow stress level close to the experimental SS curve.

Acknowledgments

The present work was supported by a grant from ONR-MURI project via University of California at San Diego where PI is Prof. S. Nemat-Nasser. The program monitor at ONR is Dr. R. Barsoum.

Appendix A

The Eshelby's inhomogeneous inclusion problem with Mori–Tanaka mean-field theory provides the total stress field given by

$$\begin{aligned}\sigma^0_{ij}+\sigma_{ij} &= \mathbf{C}^{\mathrm{m}}_{ijkl}\left[\varepsilon^0_{kl}+\bar{\varepsilon}_{kl}+\varepsilon_{kl}-\left(\varepsilon^*_{kl}-\varepsilon^{\mathrm{T}}_{kl}\right)\right]\\ &= \mathbf{C}^{\mathrm{m}}_{ijkl}\left(\varepsilon^0_{kl}+\bar{\varepsilon}_{kl}+\varepsilon_{kl}-\varepsilon^{**}_{kl}\right)\\ &= \mathbf{C}^{\mathrm{p}}_{ijkl}\left(\varepsilon^0_{kl}+\bar{\varepsilon}_{kl}+\varepsilon_{kl}\right),\end{aligned} \tag{A1}$$

where $\mathbf{C}^{\mathrm{m}}_{ijkl}$ and $\mathbf{C}^{\mathrm{p}}_{ijkl}$ are the elastic stiffness tensor of matrix and pores, respectively. σ_{ij} and ε_{kl} are stress disturbance and strain disturbance due to existence of pores, respectively. $\bar{\varepsilon}_{kl}$ is the average strain disturbance in the matrix due to the pores, and ε^*_{ij} is fictitious eigenstrain which has non-vanishing components. To facilitate the Eshelby's formula, let us introduce ε^{**}_{kl} defined by

$$\varepsilon^{**}_{kl}=\varepsilon^*_{kl}-\varepsilon^{\mathrm{T}}_{kl}. \tag{A2}$$

For the entire composite domain, the following relation always holds:

$$\sigma^0_{ij}=\mathbf{C}^{\mathrm{m}}_{ijkl}\varepsilon^0_{kl}. \tag{A3}$$

From Eshelby [10] the strain disturbance is related to ε^{**}_{mn} as

$$\varepsilon_{kl}=\mathbf{S}_{klmn}\varepsilon^{**}_{mn}. \tag{A4}$$

Requirement that the integration of the stress disturbance over the entire body vanishes leads to

$$\bar{\varepsilon}_{kl}=-f_{\mathrm{p}}(\mathbf{S}_{klmn}\varepsilon^{**}_{mn}-\varepsilon^{**}_{kl}), \tag{A5}$$

$\mathbf{S}_{\mathrm{klmn}}$ is Eshelby's tensor for pores given in Appendix B. A substitution of Eqs. (A3)–(A5)into Eq. (A1) and use of $\mathbf{C}^{\mathrm{P}}_{ijkl}=0$ (due to pore) provide a solution for ε^{**}_{kl},

$$\varepsilon^{**}_{kl}=-\frac{1}{1-f_{\mathrm{p}}}(\mathbf{S}_{klmn}-\mathbf{I})^{-1}\mathbf{C}^{m-1}_{ijkl}\sigma^0_{ij}. \tag{A6}$$

The equivalency of strain energy density of porous

$$\frac{\sigma_0^2}{2E^{\mathrm{P}}}=\frac{\sigma_0^2}{2E^{\mathrm{D}}}+\frac{f_{\mathrm{p}}}{2}\sigma_0\varepsilon^{**}_{33}, \tag{A7}$$

where the applied stress σ_0 is assumed to be along x_3-axis.

Appendix B. Eshelby's tensor for sphere inclusion

$$\mathbf{S}_{1111}=\mathbf{S}_{2222}=\mathbf{S}_{3333}=\frac{7-5v}{15(1-v)},$$

$$\mathbf{S}_{1122}=\mathbf{S}_{2233}=\mathbf{S}_{3311}=\mathbf{S}_{1133}=\mathbf{S}_{2211}=\mathbf{S}_{3322}=\frac{5v-1}{15(1-v)},$$

$$\mathbf{S}_{1212}=\mathbf{S}_{2323}=\mathbf{S}_{3131}=\frac{4-5v}{15(1-v)}.$$

References

[1] Jardine AP, Kudva JM. SPIE Proc Math Contr Smart Struct; 2712.
[2] Garner LN, Wilson LJ, Lagoudas DC, Rediniotis OK. Smart Mater Struct 2000;9:673.
[3] Martynova I, Skorohod V, Solonin S. J Phys IV 1991;C4:421.
[4] Goncharuk NV, Martynova I. Metallography 1991;4:56.
[5] Li YH, Rong LJ, Li YY. Mater Sci Forum 2002;394:511.
[6] Li YH, Rong LJ, Luo XH, Li YY. Key Eng Mater 2002;217:137.
[7] Li BY, Rong LJ, Li YY. Intermetallics 2000;8:643.
[8] Kim JS, Kang JH, Kang SB, Yoon KS, Kwon YS. Cell Met Met Foaming Technol 2003;1:1.
[9] Lagoudas DC, Entchev PB, Vandygriff EC. Proc SPIE Smart Mater Struct 2001;4333:141.
[10] Kikuchi K, Kang YS, Kawasaki A. J JPN Soc Powder and Powder Met 2000;47:302–7.
[11] Eshelby JD. Proc R Soc London, Ser A 1957;241:376.
[12] Taya M, Arsenault RJ. Metal matrix composites: thermomechanical behavior. Oxford: Pergamon Press; 1989.
[13] Mura T. Micromechanics of defects in solids. 2nd ed. The Hague: Martinus Nijihoff; 1987.
[14] Arsenault RJ, Taya M. Acta Metall 1989;35:651.
[15] Mori T, Tanaka K. Acta Metall 1973;21:571.
[16] Weng GJ. Int J Eng Sci 1984;22:845.
[17] Beveniste Y. Mech Mater 1987;6:147.
[18] Hershy AV. J Appl Mech 1954;21:236.
[19] Hill R. Phys Solids 1963;11:357.
[20] Lagoudas DC, Boyd JG, Bo Z. ASME J Mater Sci Technol 1994;116:337.
[21] Taya M, Furuya Y, Yamada Y, Watanabe R, Shibata S, Mori T. Proc SPIE 1993;1916:373.
[22] Mochida T, Taya M, Lloyd DJ. Mater Trans JIM 1991;32:931.